The Role of Halides in the Bonding and Electronic Structure of Actinyl(VI) Halides—Energy Match Driven Stability

Thomas S. Neill,* Harry Ramanantoanina,* Natalia Palina, Tim Prüßmann, Jörg Rothe, Xavier Gaona, David Fellhauer, Dieter Schild, Constantin Wansorra, Dirk Hauschild, Ralph Steininger, Bianca Schacherl, Clemens Heske, Lothar Weinhardt, Olaf Walter, Florian Weigend,* and Tonya Vitova*

ABSTRACT: The role of the equatorial ligands and their influence on the electronic structures and bonding properties of uranyl and other actinyls are not well understood and are thus at the forefront of actinide research. In the study presented here, we found that the good energy match of uranyl(VI) with F^- v alence orbitals leads to substantial changes in the uranyl electronic structure, compared to uranyl−Cl^- and uranyl−Br^-. The good energy match between uranyl(VI) and F^- likely enhances the stability of the uranyl−F^- bond, contributing to the higher U−F^- affinity in aqueous solution compared to uranyl−Cl^-/Br^-, which is also demonstrated for plutonyl(VI). These findings are based on studies of equatorial and axial ligand cov alency in three uranyl halides: $NaRb_8(UO_2)_5F_{19}\cdot 2H_2O$, $Rb_2UO_2Cl_4\cdot 2H_2O$, and $Rb_2UO_2Br_4\cdot 2H_2O$. We describe covalent uranium−halide interactions, following the trend $Br^- \approx Cl^- > F^-$. Ligand K-edge XANES and DFT (including TDDFT and LFDFT) reveal significant electronic structure differences, with the F-based compound having a uranyl-based HOMO, while Cl- and Br-based compounds show predominant ligand p character in the HOMO. A newly introduced theoretical index evaluates bond covalency. U M_4 edge HR-XANES and RIXS exhibit unexpected σ^* peak trends not directly correlated with U═O bond lengths but well explained by LFDFT RIXS calculations.

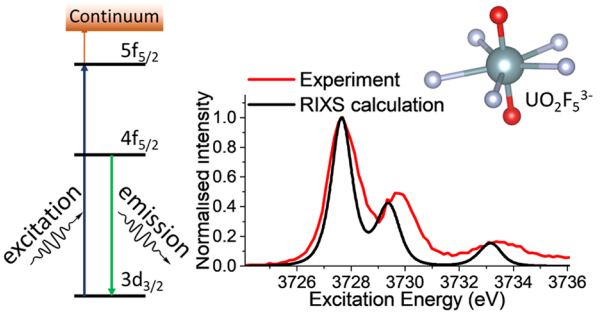

INTRODUCTION

The participation of actinide (An) 5f orbitals in An bonding remains an open question despite extensive research in the area.[1−3] Understanding the degree of the An 5f valence-orbital participation in covalent bonds informs An chemistry under a wide range of scenarios, including environmental mobility and ligand selectivity —a key factor in separation chemistry. Short-lived, α-emitting actinides also have increasing importance for targeted α-treatment of tumors. Advanced understanding of the binding behavior of the actinides to chelating ligands with novel experimental and theoretical techniques and approaches is at the forefront of research.

One of the most prevalent forms of An compounds is the actinyl series ($An(V/VI)O_2^{+/2+}$), which is the most common form of penta- and hexavalent U, Np, and Pu.[4,5] It is generally understood that the linear, axial O═An═O actinyl bond is rigidly strong, with highly covalent character, whereas equatorial ligand bonding commonly shows little to no participation of An 5f orbitals, often making these bonds labile.[2,6,7] However, recent studies have shown evidence of actinyl An-equatorial ligand covalency both experimentally and computationally.[8−10] Therefore, a comprehensive understanding of actinyl bonding, in both the axial O═An═O and equatorial directions, is required.

X-ray absorption near-edge structure (XANES) spectroscopy is an essential tool for the experimental assessment of unoccupied orbitals of An. In particular, An M_4edge high-energy-resolution X-ray absorption near-edge structure (HR-XANES) spectroscopy provides information on the relative energies of 5f δ/φ nonbonding and π- and σ-antibonding orbitals (with respect to rotation around the O═An═O bond, hereafter referred to as π^* and σ^*) of actinyl compounds.[3,6,11] Alongside advances in experimental studies, there has been significant development in theoretical chemistry to reproduce and understand the corresponding X-ray spectra of An compounds.[12−25]

In particular, assignment of spectral features has been demonstrated by density functional theory (DFT)-based calculations and more recent restricted active space self consistent field/second-order perturbation theory restricted active space (RASSCF/RASPT2) and ligand field DFT (LFDFT) calculations of 3d4f resonant inelastic X-ray scattering (RIXS) of UO_2^{2+}.[11,26,24] It has been shown in recent works that the spectral peaks exhibit strong multi-electron excitation characteristics.[19,20] For simplicity, we assign the peaks using a single-electron excitation approach. The relative energies of the peaks corresponding to 5f δ/φ nonbonding and π^* and σ^* orbitals have been shown to change based on the choice of An. It was illustrated that the length of the actinyl An═O bond can influence the peak splitting, with longer actinyl An═O bonds leading to a decreased splitting between peaks in HR-XANES that correspond to excitations into 5f δ/φ nonbonding and σ^* orbitals.[27−31] This sensitivity is due to the increased energy of the antibonding orbitals relative to the nonbonding orbitals, which was interpreted as an increase in covalency of the An═O bond.[3,6,32−35] This makes HR-XANES at the An M_4 edge a sensitive probe for the covalency of actinyl bonds. It has previously been shown that indirect influences of equatorial ligands/coordination, e.g., variations in the length of the actinyl bond, are observed using An M_4 edge HR-XANES of actinyl species.[10,30]

Given the aforementioned, uranyl halides (in particular, with F, Cl, and Br) are a promising set of compounds to study the covalency of uranyl complexes. They exhibit varied uranyl U═O bond distances: 1.81, 1.77, and 1.76 Å for U═O(F), U═O(Cl), and U═O(Br) in $Rb_2UO_2F_4{\cdot}H_2O$, $Rb_2UO_2Cl_4{\cdot}2H_2O$, and $Rb_2UO_2Br_4{\cdot}2H_2O$, respectively.[36−38] Additionally, there are differences in U−halide bond distances (2.2−2.4, 2.67, and 2.81 Å for U−F, U−Cl, and U−Br, respectively) and U coordination environments. In the solid phase, uranyl fluorides are typically pentacoordinated around the equatorial plane, compared to uranyl chlorides and bromides, which are tetracoordinated. These differences are induced by the very different properties of the halides, including their size and, therefore, charge density. Interestingly, it has been shown using relativistic quantum chemical calculations and experimental photoelectron spectroscopy that, while the covalency of An−X bonds increases along the halide series from F to I, this does not result in a stronger bond.[9]

For halide-containing samples, it is also possible to utilize ligand K edge XANES to study the metal−ligand bond covalency. While studies of lighter elements, e.g., oxygen (K edge ∼535 eV), in An compounds are limited, it is a well-established technique for the Cl K edge[6,8,39−41] and has also been applied at the Br K edge,[42] however not in the context of actinyl compounds. Ligand XANES at the Cl K edge of a series $AnCl_6^{2-}$ compounds has highlighted the importance of energy-degeneracy driven covalency of 5f orbitals in An;[43] however, this has been contested.[16] Nuclear magnetic resonance (NMR) and nuclear quadrupole resonance (NQR) investigations of $Cs_2UO_2Cl_4$ and $Cs_2UO_2Br_4$ suggest higher electric field gradients along the U−halide bond for bromide vs chloride, consistent with higher covalency in the uranyl bromide system.[44] These results provide strong evidence of orbital mixing between An 5f and halide p orbitals. However, direct comparisons between uranyl fluoride, chloride, and bromide bonding using advanced X-ray spectroscopic techniques applied from both the metal and the ligand perspective are missing.

In this study, we investigate three uranyl halides ($NaRb_8(UO_2)_5F_{19}{\cdot}2H_2O$, $Rb_2UO_2Cl_4{\cdot}2H_2O$, and $Rb_2UO_2Br_4{\cdot}2H_2O$) using a range of spectroscopic and computational techniques, resulting in a comprehensive study of the electronic structure and bonding properties of these actinyl halides. For this purpose, a combination of U M_4 edge HR-XANES, U 3d4f RIXS, F and Cl K edge XANES, Br K edge HR-XANES, X-ray photoelectron spectroscopy (XPS), extended X-ray absorption fine structure (EXAFS), and computational approaches, i.e., LFDFT and time-dependent DFT (TDDFT), has been employed. Using three different synchrotron radiation beamlines at the KIT Light Source (the INE-Beamline,[45] the ACT station at the CAT-ACT beamline,[27,46,47] and the X-SPEC beamline[48]), we identify unexpected spectral trends in the U M_4 edge HR-XANES (RIXS) spectra and demonstrate equatorial ligand-uranium covalency in Br, Cl, and F uranyl complexes. The electronic structures of these complexes are studied in view of the bond covalency and bond stability of the uranyl−halide bond. This new insight is then applied to EXAFS investigations of the complexation strength of halides (F, Cl, and Br) to aqueous U(VI) and Pu(VI), thereby aligning actinyl bonding properties and ligand affinity in aqueous complexes.

RESULTS AND DISCUSSION

Structural Characterization of Uranyl Halides. Single crystal XRD results show the successful synthesis of $Rb_2UO_2Cl_4{\cdot}2H_2O$ and $Rb_2UO_2Br_4{\cdot}2H_2O$ (Table S2).[37,38] Initial Br precipitates also contained significant contributions of a RbBr contamination. With further crystallization, pure $Rb_2UO_2Br_4{\cdot}2H_2O$ crystals were formed, as verified by single crystal XRD. Initial $NaRb_8(UO_2)_5F_{19}{\cdot}2H_2O$ powder XRD did not correspond to any previously published data, and thus single-crystal diffraction was used to resolve its structure. It contains a uranyl coordination similar to other uranyl fluorides, such as $Rb_2UO_2F_4{\cdot}2H_2O$.[36] Significantly, the rubidium uranyl fluoride has a U−F coordination of 5, whereas the rubidium uranyl chloride and bromide phases have U−Cl and U−Br coordination of 4. The single-crystal data for $NaRb_8(UO_2)_5F_{19}{\cdot}2H_2O$, $Rb_2UO_2Cl_4{\cdot}2H_2O$, and $Rb_2UO_2Br_4{\cdot}2H_2O$ are listed in Table S3 and their unit cells are shown in Figure S2. SEM images (Figure S3) show differences in the size and morphology for the three successfully synthesized uranyl halides. The results of the EXAFS analysis of the samples (Figure S4, Table S3) are in close agreement with the XRD outcomes (Figure 1); U═O and U−X bond distances are similar within the uncertainties of the two techniques. Combined, these techniques confirm the successful synthesis of three solid phases: $Rb_2UO_2Cl_4{\cdot}2H_2O$, $Rb_2UO_2Br_4{\cdot}2H_2O$, and $NaRb_8(UO_2)_5F_{19}{\cdot}2H_2O$. The interatomic distances for these phases are shown in Figure 1 and listed in Table S4. The Br and Cl phases are isostructural and in agreement with previously published data.[37,38] There is one U site present in each of the structures, coordinated with two axial oxygens and four equidistant equatorial halide ions in D_{4h} symmetry.[37,38] The F phase has a unique structure with three distinct U sites. These three sites all have a similar coordination of 5 F ions (at different interatomic distances) and two uranyl O, which can be approximated by D_{5h} symmetry. In all three sites, the U═O distances are longer than those in the $Rb_2UO_2Cl_4{\cdot}2H_2O$ and $Rb_2UO_2Br_4{\cdot}2H_2O$ structures. This is consistent with other Rb

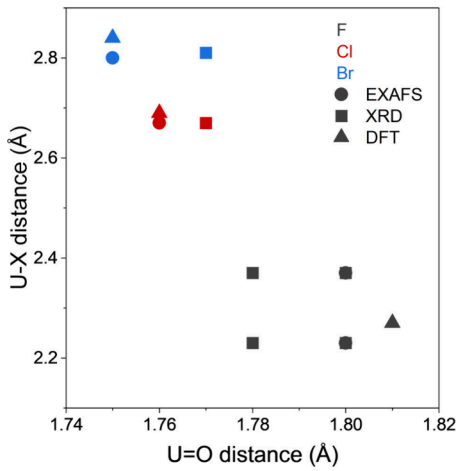

Figure 1. U−halide (U−X) bond distances as a function of U═O uranyl bond distances for the three different compounds $NaRb_8(UO_2)_5F_{19}\cdot 2H_2O$ (F), $Rb_2UO_2Cl_4\cdot 2H_2O$ (Cl), and $Rb_2UO_2Br_4\cdot 2H_2O$ (Br), based on EXAFS analyses, single crystal X-ray diffraction (XRD) data, and density functional theory (DFT) calculations (errors for these values can be found in Table S4). Multiple points for F correspond to a range of different interatomic distances and crystallographic sites. These were averaged for EXAFS fitting and symmetry constrained for DFT values, resulting in fewer points for these approaches.

uranyl fluorides.[36] In general, the uranyl U═O bond distances follow the trend U═O(F) > U═O(Cl) ≈ U═O(aq) > U═O(Br). The DFT-based calculations found bond distances similar to the experimentally obtained values, as shown in Figure 1.

U M_4 Edge HR-XANES. Figure 2a shows the molecular orbital scheme of uranyl $(O{=}U{=}O)^{2+}$. The unoccupied states in this scheme can be probed by XANES from the viewpoint of a chosen atomic species and its localized core hole. For U, the U M_4 edge is well-suited for probing states with p and f symmetry. However, traditional U M_4 edge XANES spectra, recorded in total fluorescence yield (TFY) as a function of excitation energy, are broad due to the significant lifetime broadening of the U $3d_{3/2}$ core level in the final state of the absorption process (best described by a Fermi's Golden Rule approach).

In contrast, HR-XANES spectra can be collected with a resolution considerably below the lifetime broadening of the U 3d core level. This is done by recording the X-ray emission intensity at a fixed emission energy, here at the maximum of the normal, "nonresonant" emission spectrum (further details in Supporting Information). Probing only a specific decay channel removes the impact of the lifetime broadening in the (now) intermediate state of the excitation−deexcitation process. This corresponds to a RIXS process, best described by the Kramers−Heisenberg formalism (see eq S1). In conjunction with Figure 3 (below), we will discuss that such an HR-XANES spectrum merely constitutes a specific cut through the more detailed RIXS map, which then gives the full electronic and chemical structure information as viewed from the perspective of a specific core hole.

U M_4 edge HR-XANES results for the three uranyl halides can be seen in Figure 2b−d and Figure S5, measured as described above. These are presented alongside two-component TDDFT XANES simulations employing the exact two-component decoupling (X2C) approach for relativistic effects (hereby simply called TDDFT). The TDDFT results for $UO_2F_5^{3-}$, $UO_2Cl_4^{2-}$, and $UO_2Br_4^{2-}$ are given in Figure 2e−g, representing the coordination environments of $NaRb_8(UO_2)_5F_{19}\cdot 2H_2O$, $Rb_2UO_2Cl_4\cdot 2H_2O$, and $Rb_2UO_2Br_4\cdot 2H_2O$. Calculations were also carried out on the $UO_2F_4^{2-}$ moiety as a direct comparison to the Cl and Br structures but with very little difference between $UO_2F_5^{3-}$ and $UO_2F_4^{2-}$ observed in both spectra and orbital populations (Figure S6, Table S5). In the following, the orbital groups corresponding to peaks in the experimental and calculated U M_4 edge spectra will be referred to as A, B, and C, which correspond to excitations into δ_u and φ_u (A, mainly nonbonding), π_u^* (B, antibonding), and σ_u^* (C, antibonding) orbitals, respectively, as labeled in Figure 2a. All three peaks in the experimental spectra are reproduced in the TDDFT

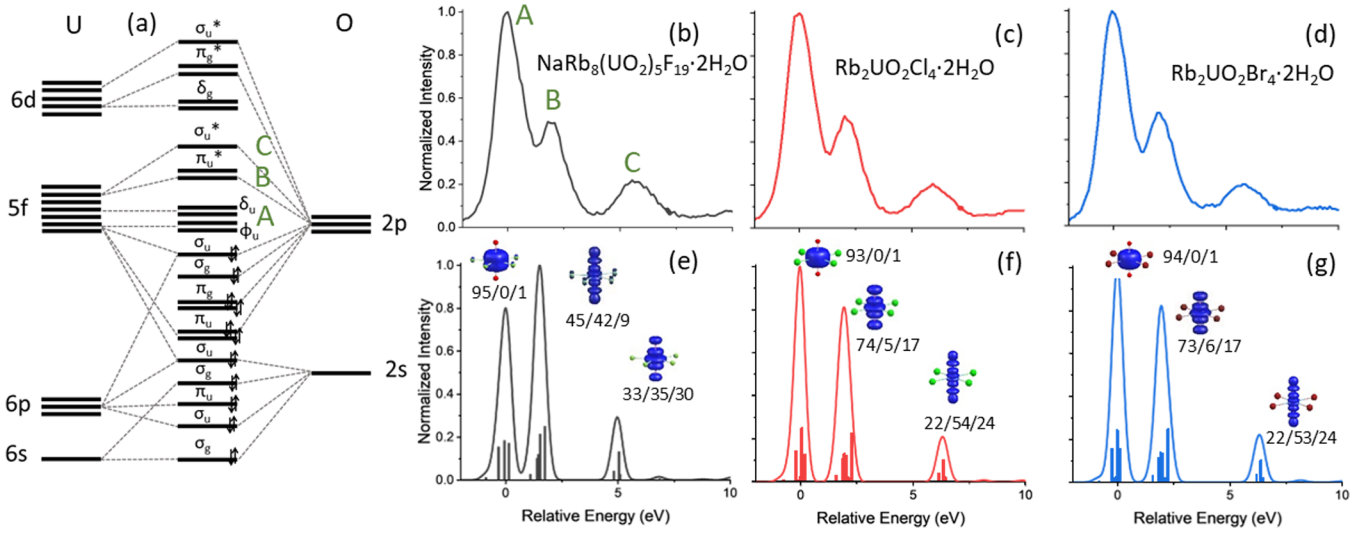

Figure 2. Schematic MO diagram of $U(VI)O_2^{2+}$, including orbitals corresponding to features A, B, and C observed in U M_4 edge HR-XANES (a), adapted from ref 7, Copyright 2007 American Chemical Society. Experimental U M_4 edge HR-XANES for $NaRb_8(UO_2)_5F_{19}\cdot 2H_2O$ (including labels for A, B, and C peaks) (b), $Rb_2UO_2Cl_4\cdot 2H_2O$ (c), and $Rb_2UO_2Br_4\cdot 2H_2O$ (d). TDDFT calculated U M_4 edge XANES, including only the major excited state character contributions in % (U f/U p/O p) for $UO_2F_5^{3-}$ (e), $UO_2Cl_4^{2-}$ (f), and $UO_2Br_4^{2-}$ (g).

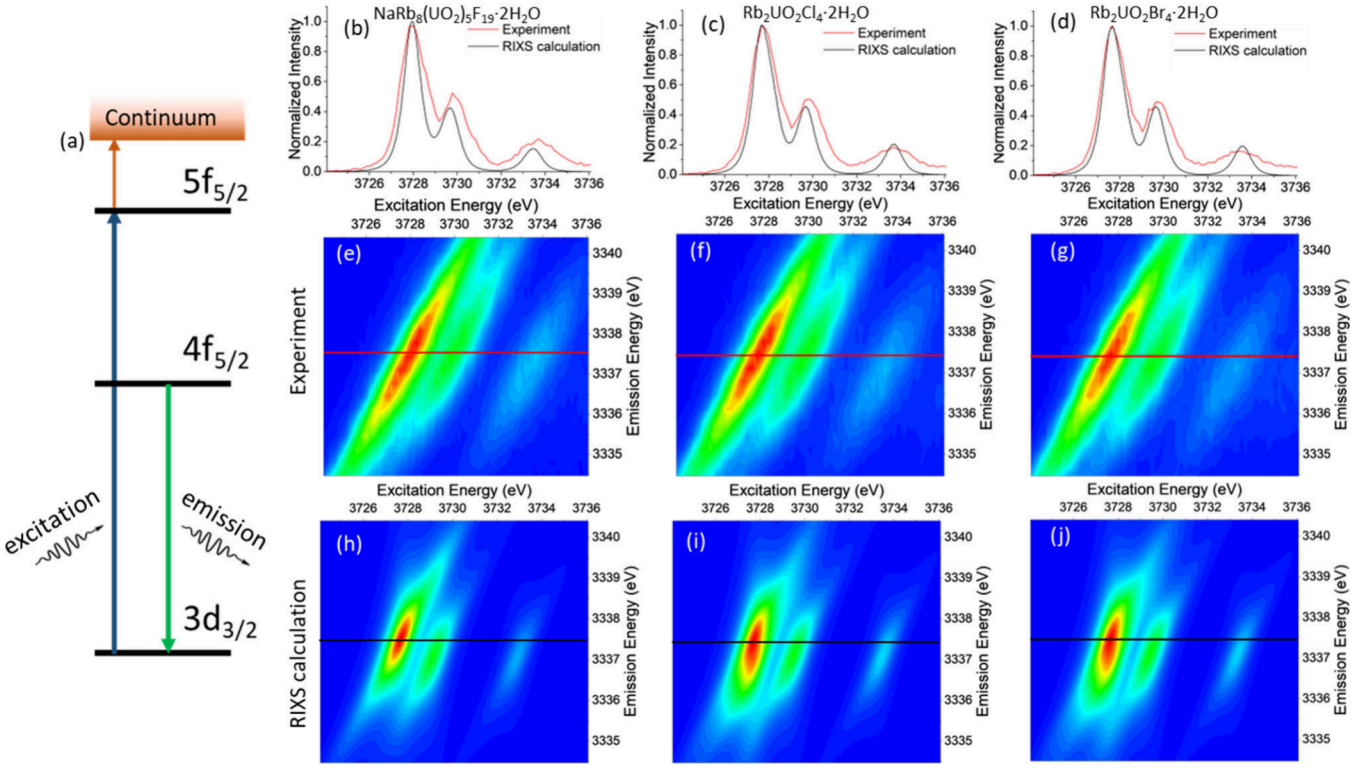

Figure 3. Schematic representation of the excitation and emission processes for 3d4f RIXS (a). Normalized resonance cross sections at the highest-intensity emission energy for $NaRb_8(UO_2)_5F_{19}\cdot 2H_2O$ (b), $Rb_2UO_2Cl_4\cdot 2H_2O$ (c), and $Rb_2UO_2Br_4\cdot 2H_2O$ (d). Experimental (e–g) and calculated (h–j) 3d4f RIXS maps for $NaRb_8(UO_2)_5F_{19}\cdot 2H_2O$ (e, h), $Rb_2UO_2Cl_4\cdot 2H_2O$ (f, (i), and $Rb_2UO_2Br_4\cdot 2H_2O$ (g, j). The cross sections presented in (b)–(d) are shown as red and black horizontal lines ("cuts") in the RIXS maps in (e)–(j).

calculations, and the calculated charge transfer upon excitation for each band is given by the weighted sum of the densities of excited state contributions to each band in Figure 2e–g. Peak A is dominated by transitions to unoccupied δ/φ orbitals with mainly U 5f character, and the peak maximum shifts to lower energies from F to Cl and further to Br (to a lesser extent) in both calculated and experimental spectra (Figure S5). This trend suggests that increasing the electron density at the U site is consistent with the relative electronegativities of the equatorial ions (Pauling electronegativity F > Cl > Br). Peak B is attributed to transitions to a π^*-type spinor state with contributions from U 5f, U 6p, and O 2p. It is higher in energy than A by ~2 eV. Peak C results from transitions to the σ^*-type spinors, again with contributions from U 5f, U 6p, and O 2p.

In our TDDFT XANES calculations, we find a clear trend of increasing A–C peak separation with decreasing uranyl U=O bond distance ($A-C_F$ = 5.1 eV, $A-C_{Cl}$ = 6.3 eV, and $A-C_{Br}$ = 6.4 eV, Table S5). This trend is not reflected in the experimental HR-XANES data, where the separations between peaks A and C are $A-C_F$ = 5.6 eV, $A-C_{Cl}$ = 5.9 eV, and $A-C_{Br}$ = 5.7 eV (estimated error of ±0.05 eV), suggesting that there is no clear correlation between the HR-XANES A-C peak separation and U=O bond distance in these uranyl halide systems. As mentioned, this is likely caused by the differences in the final states of XANES (as calculated with TDDFT) and HR-XANES (i.e., a cut from a RIXS map); in contrast, our LFDFT RIXS calculations reproduce the peak positions in the experimental HR-XANES spectra very well (Figure 3). These results highlight that caution should be taken when comparing spectral trends of HR-XANES (i.e., RIXS) with traditional XANES, since fundamentally different processes are being probed.

U 3d4f RIXS. In U M_4 edge 3d4f core-to-core RIXS, the excitation by an incident photon is accompanied by the emission of a second photon. This involves the ground state as the initial state, the core-excited state as the "intermediate state", and a final state characterized by a U 4f hole and an excited electron in the U 5f-derived states, as depicted in Figure 3a. The data can be plotted in a RIXS map, where the emission intensity is shown as a function of excitation and emission energies (cf. Figure 3a). Experimental RIXS data for the 3 uranyl halides are shown in Figure 3e–g, alongside RIXS calculations performed using LFDFT (Figure 3h–j), whereby the core holes in both intermediate (3d) and final state (4f) are considered. HR-XANES spectra correspond to horizontal cuts through the RIXS maps, taken at the resonance maximum (i.e., corresponding to excitation energy scans taken at the emission energy with the maximum intensity). A comparison of these calculated and experimental RIXS map cuts (i.e., HR-XANES spectra) is shown in Figure 3b–d. As already mentioned, the theoretical calculations replicate the experimental data closely, both in terms of relative energy positions and intensities and with all spectral features of the experimental RIXS maps shown in the calculated maps as well. Next, we investigate the energy shift of the emission maximum between nonresonant ($h\nu$ = 3780 eV) and resonant (i.e., at the maximum emission intensity of the RIXS map) excitation. This shift in energy is caused by the presence of a "spectator" electron in the final state for resonant excitation, in contrast to the ionized final state for nonresonant excitation. Such shifts have been observed for 3d, 4f, and 5f elements previously.[3,29,49−53] In

this study, the experimental energy shifts are very similar for all three samples. For the F compound, the energy shift is 0.48 eV, for Cl 0.44 eV, and for Br 0.45 eV. These values are very similar, i.e., without a clear trend in the energy shift for the 3 samples. It has previously been suggested that the magnitude of the energy shift depends on the orbital delocalization of the unoccupied 5f states, where a larger energy shift suggests greater orbital localization.[3] The present results thus indicate that the degrees of delocalization of the unoccupied 5f states are similar for the three investigated samples.

As discussed above, the LFDFT RIXS calculations are more successful in reproducing the acquired experimental HR-XANES spectra than the TDDFT XANES calculations, demonstrating the difference between TFY XANES/transmission-mode XANES (XANES) and HR-XANES (RIXS). Figure 4 illustrates the trends in the A−C peak separation for

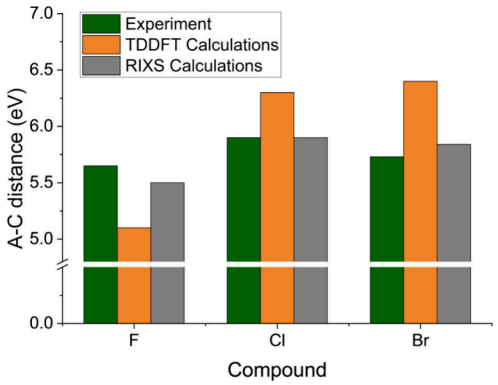

Figure 4. Comparison of A−C peak energy separation (distance) for $NaRb_8(UO_2)_5F_{19}\cdot 2H_2O$ (F, left), $Rb_2UO_2Cl_4\cdot 2H_2O$ (Cl, center), and $Rb_2UO_2Br_4\cdot 2H_2O$ (Br, right), using experimental data (green), TDDFT calculations (orange), and LFDFT RIXS calculations (gray).

the experimental data and the two computational approaches. The A−C peak distances are very similar for the experimental and LFDFT-calculated RIXS spectra, demonstrating that the RIXS final state is dominated by the U 4f hole, which is not considered in the TDDFT calculations presented here. This is an important consideration when replicating experimental XANES and HR-XANES (RIXS) spectra. Interestingly, several experimental works have suggested that clear trends between uranyl U═O bond lengths and U M_4 edge HR-XANES A-C peak separation exists.[27,28,30,31] In our case, this trend was only observed with the TDDFT XANES calculations (Figure 2), while it is not present in experimental or calculated RIXS of the uranyl halide systems (<0.3 eV change in the A-C peak distance across the halide series). The (more comprehensive) RIXS results thus suggest that a more complex relationship between the A-C peak separation and uranyl bond length exists than previously demonstrated.

Halide K Edge XANES/HR-XANES. In order to further investigate U−halide bonding, halide K edge XANES spectra of $NaRb_8(UO_2)_5F_{19}\cdot 2H_2O$ and $Rb_2UO_2Cl_4\cdot 2H_2O$, as well as HR-XANES (RIXS) of $Rb_2UO_2Br_4\cdot 2H_2O$ were measured and are shown in Figure 5a−c. In all three spectra, we find pre-edge features for the uranyl halide but not for the corresponding salts (KBr, CsCl, RbF; Figure S10). Previous characterization of $[PPh_4]_2UO_2Cl_4\cdot 2H_2O$ identified these pre-edge features as a mixing between the Cl 3p, U 5f, and U 6d orbitals;[8] the presence of pre-edges in all investigated compounds thus suggests significant mixing between halide p and U 5f/6d orbitals. The HR-arrangement (RIXS) was used for the Br K edge to avoid the larger core-hole lifetime broadening effects of XANES. Previous publications have highlighted the importance of using HR-XANES to separate the Br K-edge pre-edge features from the white line and demonstrated that the spectral features are comparable between standard XANES and HR-XANES (RIXS).[54,55] Therefore, for the qualitative assessment

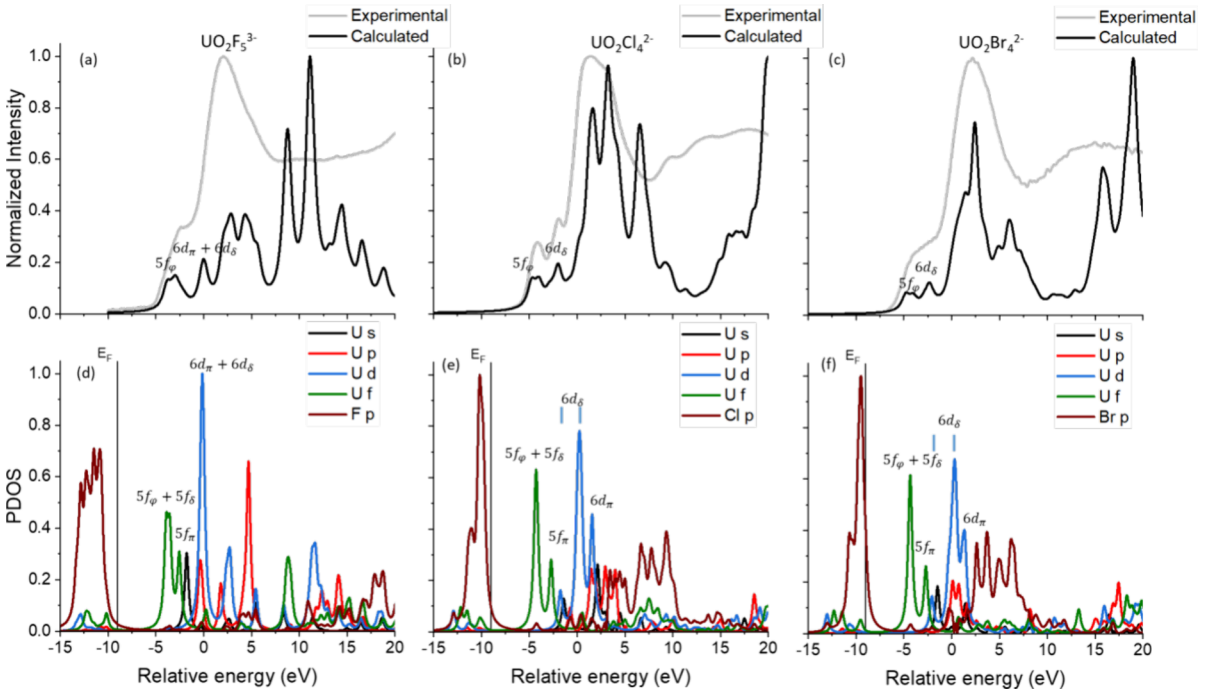

Figure 5. Experimental and calculated halide (F/Cl/Br) K edge XANES of $NaRb_8(UO_2)_5F_{19}\cdot 2H_2O$ (a), $Rb_2UO_2Cl_4\cdot 2H_2O$ (b), and HR-XANES (RIXS) of $Rb_2UO_2Br_4\cdot 2H_2O$ (c). TDDFT partial density of states (PDOS) calculations are shown in (d)−(f).

of the spectral features discussed here, Br K-edge HR-XANES is the most suitable experimental approach.

In Figure 5a–c, the energy axis of the experimental spectra is given such that 0 eV corresponds to the energy of the first inflection point of the absorption edge. The TDDFT-calculated spectra (Figure 5d–f) are shifted in energy to best match the experiments and are obtained by broadening the oscillator strengths of the electron transitions with a Lorentzian function with a half-width-at-half-maximum parameter of 0.5 eV. The pre-edge features of the ligand K edge spectra are well reproduced by the TDDFT calculations in terms of relative excitation energies and intensities. These pre-edge spectral features involve transitions from the ligand 1s electrons to the unoccupied metal-based molecular orbitals mixed with halide p contribution, and the calculated double pre-edge peaks in the theoretical spectra correspond to valence molecular orbitals with predominant $(UO_2)^{2+}$ 5fφ and 6dδ characters.

To assess the strength of the covalent bonding interaction between the $(UO_2)^{2+}$ fragment and the equatorial ligands, Figure 6 and Table S9 depict the ligand contribution to key

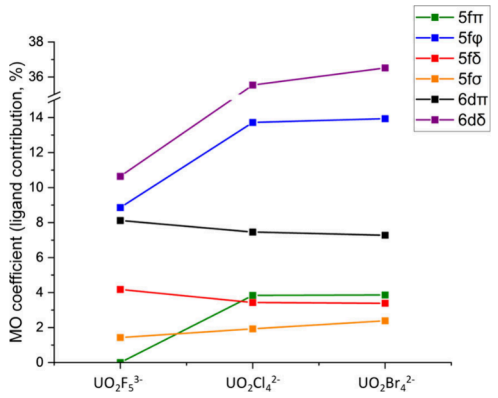

Figure 6. Halide contributions to the molecular orbital coefficients for the unoccupied 5fδ, 5fφ, 5fπ, 5fσ, 6dπ, and 6dδ orbitals.

molecular orbitals, i.e., φ_u (5fx, 5fy) and δ_g (6dxy, 6dx^2-y^2), which are nonbonding in the UO_2^{2+} fragment and primarily serve as the equatorial ligand-acceptor orbitals. In the case of $UO_2Br_4^{2-}$ and $UO_2Cl_4^{2-}$, the δ-type 6d orbitals of UO_2^{2+} interact the most with equatorial ligands forming unoccupied molecular orbitals with b_{1g} and b_{2g} symmetry in the D_{4h} point group, because their lobes intercept the symmetry-adapted linear combination of p orbitals on the halide ions. The φ-type 5f orbitals of $(UO_2)^{2+}$ also have a sizable interaction with the equatorial ligands forming unoccupied molecular orbitals with the double-degenerate e_u symmetry in D_{4h}. Besides, the degeneracy of the δ-type 5f orbitals is lifted in D_{4h}, transforming it to the b_{1u} and b_{2u} molecular orbitals. The b_{2u} orbital with predominant 5fz(x^2-y^2) character has a minor interaction with the equatorial ligands. In contrast, the b_{1u} orbital with predominant 5fxyz character conserves the nonbonding nature, as it is in the formal $(UO_2)^{2+}$ fragment.

In the case of $UO_2F_5^{3-}$, the 5f orbitals show similar characteristics as described above, except that, due to the symmetry restriction of the D_{5h} point group, the δ-type 5f and 6d orbitals remain 2-fold degenerate when transitioning from UO_2^{2+} to $UO_2F_5^{3-}$. However, the qualitative diagram of the 6d splitting exerted by the fluoride ligand field follows a different sequence. Note that the sequences 6dδ, 6dπ, and 6dσ (ordered in terms of MO energy) arise from the UO_2^{2+} fragment, and the same sequence is found in $UO_2Br_4^{2-}$ and $UO_2Cl_4^{2-}$. In $UO_2F_5^{3-}$, the lowest-energy 6d-type molecular orbitals correspond to the π type, and the 6dδ is shifted to higher energy by 0.5 eV. This is possible because 6dδ and 5fφ have the same irreducible representations in D_{5h} (e_2'), so they can mutually interact forming 5fφ/6dδ hybridized orbitals in fluoride. The calculation shows that, in the ground state, the 5fφ orbitals have 1.4% character of 6dxy and 6dx^2-y^2 in $UO_2F_5^{3-}$. This means that the calculated second pre-edge peak for the fluoride case represents, in fact, contributions from both 6dπ and 6dδ orbitals, and the peak arising from 6dπ states merges with the absorption edge for the chloride and bromide analogs. Comparing ground- and excited-state calculations (Table S9), the same overall trend discussed above is seen for both sets of calculations.

Overall Bonding Analysis of Uranyl Halides. For investigating trends in uranyl halide bonding, the molecular orbitals and the ground state density obtained at a one-component level were investigated with different tools: Mulliken population analysis (MPA),[56] natural population analysis (NPA),[57] and population analysis based on occupation numbers (PABOON).[58] In addition, charges were determined to best reproduce the electrostatic potential (ESP).[59] Further details on all of these approaches are provided in the Supporting Information. The results for these analyses are shown in Figure S7 and Table S6; clear trends are observed for all analyses, with a significant lowering of the positive partial charge of U when going from F to Cl. This comes with a decrease of charge mainly located at X, according to NPA, or at O, according to MPA, or both, according to PABOON and ESP. Taking the difference of partial charges as (part of) a measure for covalency, also these methods confirm the increase of covalency for the U–O bonds and also in the U–X bonds from F to Cl (with Cl to Br yielding similar degrees of covalency).

Specific information about the character of σ- and π-type bonds was obtained from analysis of Pipek-Mezey localized molecular orbitals (LMOs).[60] For all cases, one lone pair (LP) and one σ-type bond to U for each O and X atom, as well as two additional π-type orbitals, were found. For the X atoms, these are mainly localized at X, while they are somewhat delocalized toward U for the O atoms (see Figure S8). The degree of delocalization, and thus the covalency/polarization of the U–O bond, depends on the halide and, if measured by the Mulliken population, increases from F to Br. The population at O (as a fraction of 1) decreases from 0.71 to 0.67 for the LMO representing the U–O σ-bond and from 0.84 to 0.80 for each of the two MOs representing the U–O π bonds; see Table S7. Additionally, the Mulliken overlap population (as a fraction of 1) may be employed as a measure of the interaction strength, which increases from 0.15 to 0.19 for the U–O σ bond and from 0.13 to 0.15 for the U–O π bonds (from F to Br). One might combine the two numbers to get a measure for the total covalent interaction strength in a simple manner, γ_{LU}, the covalency index (CVI), which can be defined as

$$\gamma_{LU} = S_{LU}\cdot\left(1 - \left|\frac{Q_L - Q_U}{Q_L + Q_U}\right|\right) \quad (1)$$

with Q_L and Q_U being the Mulliken gross population for ligand and uranium, respectively, and S_{LU} being the overlap population of the localized MOs. γ_{LU} is designed in a way that it is identical to S_{LU} if $Q_L = Q_U$ (maximum covalency) and

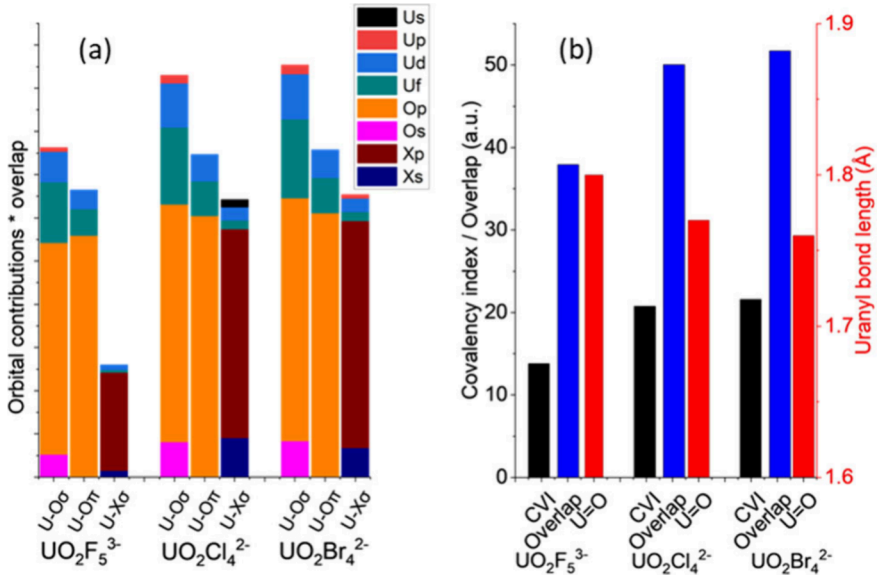

Figure 7. Mulliken gross population contributions of uranium s (black), p (red), d (blue), and f (green), oxygen p (orange) and s (pink), as well as halide X p (brown) and s (dark blue) to localized U−O and U−X molecular orbitals of $UO_2F_5^{3-}$, $UO_2Cl_4^{2-}$, and $UO_2Br_4^{2-}$. Mulliken gross population values are multiplied by the overlap populations between U and O, or U and X, as relevant (a). Total summed covalency index (CVI)/overlap summed over localized molecular orbitals (left axis) and U═O interatomic distances of $UO_2F_5^{3-}$, $UO_2Cl_4^{2-}$, and $UO_2Br_4^{2-}$ (right axis) (b).

approaches zero (i.e., no covalency) for $Q_L \gg Q_U$ or $Q_L \ll Q_U$. These results are shown in Figure 7, summarized in Table S7, and discussed below. Note that this quantity is conceptionally different from the orbital mixing coefficient λ proposed previously.[2,43] Whereas the latter intends to predict bond properties of the composed system from the properties (in particular, the orbital energies) of separate ions M^{6+} and X^-, the CVI is based on the converged orbitals of the entire $UO_2X_4^{2-}$ or $UO_2X_5^{3-}$ moieties and thus just "translates" their electron distribution to simple numbers representing the degree of covalency.

For the LPs and the π-type orbitals at X (LMOs X1 and X3 in Figure S8), the CVI is below 0.01, suggesting no covalency for these orbitals (as expected). For X = F, the remaining U-X LMO (X2 in Figure S8) may also be considered closer to an LP than a σ bond, as here the CVI is not significantly larger than for the LPs. This is different for X = Cl, Br, where the CVI $\geq$ 0.03. For the π component of the U−O bonds (O3 in Figure S8), CVI increases from 0.042 to 0.059, and for the σ part (O2 in Figure S8) from 0.088 to 0.120; thus, covalency is increasing for both the σ and the π parts of this bond, from $UO_2F_5^{3-}$ via $UO_2F_4^{2-}$ and $UO_2Cl_4^{2-}$ to $UO_2Br_4^{2-}$. For comparison, in UO_2^{2+}, CVI is 0/0.188/0.083 for LP/σ/π, which is significantly higher than those for the four halide compounds for σ/π. We note that these numbers do not dramatically depend on the length of the U−O bond: if the U−O bond is elongated by 11.9 pm to the value in $UO_2F_5^{3-}$, then CVI becomes 0/0.176/0.084. Thus, according to all analyses, the presence of halides reduces the covalency of the U−O σ and π bonds, with the size of this reduction increasing with the electronegativity and the number of halide bond partners. In turn, with decreasing covalency, U−O distances increase from 169.2 pm for UO_2^{2+} via 175.5 pm for $UO_2Br_4^{2-}$, 175.9 pm for $UO_2Cl_4^{2-}$, and 180.1 pm for $UO_2F_4^{2-}$, to 181.1 pm for $UO_2F_5^{3-}$.

Character of the HOMO. Figure 8 shows the density of states (DOS) of the highest occupied molecular orbitals (HOMOs) using DFT, and Figure S9 shows the contributions

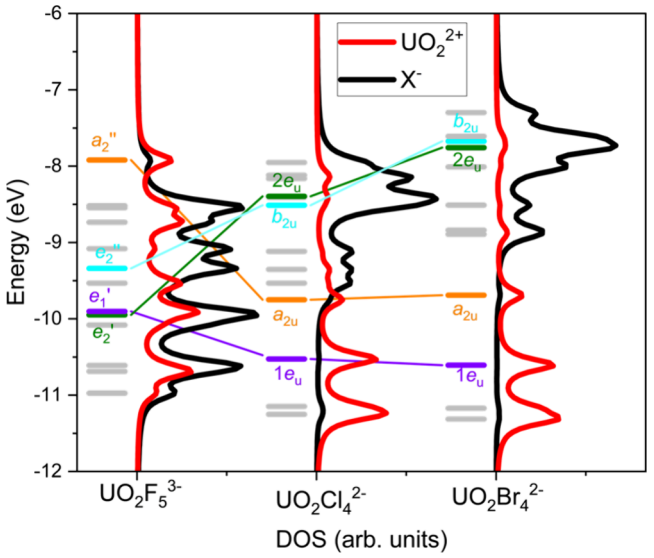

Figure 8. DFT density of states (DOS) calculations for $UO_2F_5^{3-}$, $UO_2Cl_4^{2-}$, and $UO_2Br_4^{2-}$ showing the halide (X^-) and uranyl (UO_2^{2+}) contributions to the total DOS, in the energy region that corresponds to the upper highest occupied molecular orbitals (HOMOs). Key MOs are highlighted in orange, cyan, purple, and green.

to occupied and unoccupied states for the $UO_2Br_4^{2-}$, $UO_2Cl_4^{2-}$, and $UO_2F_5^{3-}$ structures, as well as electron densities of key 5fσ contributors calculated using TDDFT. There are significant differences between the $UO_2F_5^{3-}$, $UO_2Br_4^{2-}$, and $UO_2Cl_4^{2-}$ electronic structures (Figure 8). In particular, there is an increased mixing between uranyl and F^-, compared to Cl^- and Br^-, in the upper HOMOs. The character of the $UO_2F_5^{3-}$ 5fσ orbitals (for which the canonical orbital schemes are shown in Figure S9) is very different from those in $UO_2Br_4^{2-}$ and $UO_2Cl_4^{2-}$. In $UO_2F_5^{3-}$, the HOMOs are of mixed O 2p, U 5f, U 6p, and F 2p covalent character, whereas

in $UO_2Br_4^{2-}$ and $UO_2Cl_4^{2-}$, the HOMOs have predominant Br 4p and Cl 3p contributions, respectively. This significant change in the electronic structure of the three compounds is caused by the lower energy 2p orbitals of F, compared with Cl 3p and Br 4p. It likely contributes to the apparently anomalous trend in the A−C peak separation, both experimentally and with LFDFT RIXS calculations, for the three compounds. Due to the higher energy a_2'' orbital with significant 5fσ character, an increased "pushing-from-below" effect in the fluoride system is observed. TDDFT and LFDFT calculations reveal that there is a covalent attractive contribution to the uranium−halide bonding interaction (Tables S5−S9; Figure 6, Figure S6). While the bonding analysis suggests that the covalent interactions are more prevalent in the chloride and bromide systems, the fluoride ligands have the largest effect on the uranyl electronic structure (Figure 8, Figure S9). The "pushing-from-below" effect increases the energy of the uranyl 5fσ_u orbital due to U semicore 6p participation.[7,61] In the fluoride system, this orbital is pushed even higher in energy to become the HOMO, due to an equatorial ligand "pushing" effect. This, in turn, leads to a net repulsion molecular orbital interaction with the σ^* orbital and therefore would result in a larger A−C separation than would otherwise be expected, considering the U═O bond distance alone. Furthermore, mixing of unoccupied orbitals on the uranyl fragment is influenced by the equatorial ligands. Thus, in the fluoride system, the contribution of U 5f in the σ^* orbitals is larger than in the other halide systems (see Table S9), which may contribute to a larger A−C separation in the HR-XANES. In order to directly compare uranyl-halide interactions in isostructural environments, Figure S11 also shows the DOS of the HOMOs for $UO_2F_4^{2-}$. Here, the DOS of $UO_2F_4^{2-}$ more closely relates to that of $UO_2F_5^{3-}$ than $UO_2Cl_4^{2-}$ and $UO_2Br_4^{2-}$, in particular the key MOs highlighted in Figures 8 and S11. This confirms that the changes in DOS and resulting bonding properties are more affected by halide (F^- vs Cl^- or Br^-) than by equatorial coordination number.

L_3 Edge EXAFS and M_4 Edge HR-XANES of U and Pu Solution Samples. In order to probe the bond strength of the actinyl halide systems, comparative studies of solution samples were also conducted. Solutions of U(VI) (10 mM) and Pu(VI) (5 mM) in 0.1 M acid were prepared as follows: HF/NaF (0.1−1 M F^-), HCl/NaCl (2−6 M Cl^-), and HBr/NaBr (2−6 M Br^-), and the local coordination environment of U/Pu was investigated by using U/Pu L_3 edge EXAFS. Here, a clear preference is shown for U/Pu−F bonding (compared to U−Cl and U−Br bonding). EXAFS fitting (Figures S12 and S13, Tables S10 and S11) illustrates that U(VI) is predominantly complexed to F at concentrations as low as 0.1 M (average coordination $UO_2F_3(H_2O)_2$), which is supported by thermodynamic results (Figure S14). Fitting of EXAFS for Pu(VI) in 1 M F solution suggests that F complexes more strongly than Cl and Br, and the extent of complexation is comparable to that of the U(VI) system ($PuF_{3.5}O_{2.5}$ is the average coordination in this case). In contrast, for Cl, the average coordination is $UO_2Cl_{1.7}(H_2O)_{2.9}$ and $PuO_2Cl_{1.3}(H_2O)_{3.6}$ even at 6 M Cl, and low halide coordination is also observed for the U(VI)-Br system at 2 M Br $UO_2Br_{0.5}(H_2O)_{4.5}$. It was not possible to measure higher Br concentrations or Pu(VI)-Br systems in solution due to the strong absorbance of fluorescent X-rays by Br. These investigations into solution complexes are in good agreement with previous studies[62,63] and demonstrate that the bonds between uranyl/plutonyl and F are stronger and exhibit higher stability than uranyl/plutonyl-Cl or Br bonds.

M_4-edge HR-XANES spectra of U and Pu halide solutions were also measured. As discussed in more detail in the methods section of the Supporting Information, the solution samples were affected to different degrees by radiation damage. In Figure S1, the spectra with negligible (for U(VI) in 0.1 M F^-) and extensive (for U(VI) in 1 M F^-) radiation damage are shown. For U(VI), only the 0.1 M F system shows significant variation in the spectral profile, with a decrease of the energy gap between the first and third peaks (A−C energy distance) (Figure S15). The decrease in the A−C peak distance is likely caused by the change in coordination environment in conjunction with strong complexation of F^- ions to the U(VI) center and can be linked to the increase in U═O uranyl bond length observed in the EXAFS fitting. A similar change is also observed in the Pu 1 M F system, which might, however, also be caused by radiation induced damage (Figure S16).

Evaluation of Relations between U−Halides/O Covalency and Bond Length. All halide K edge XANES spectra show evidence of covalent contributions to U−halide bonding. The evaluation of halide p-orbital mixing in unoccupied uranyl-based canonical orbitals illustrates that the bond covalency for 5f-based uranyl orbitals is in the order Cl ≈ Br > F (Figure 6). This is consistent with the multiapproach bond analysis, and when all mixing coefficients are summed up for both 5f and 6d orbitals, the covalency for the uranyl−F and U═O(F) bonds is smaller than for the respective interaction between uranyl and Cl/Br. The analysis of the localized valence orbitals concerning Mulliken overlap and contributions from the two bond partners (considered either separately or in the newly proposed CVI) is depicted in Figure 7a. It illustrates that the orbital overlap and mixing of halide/O p with U 5f/6d orbitals increases in the order F < Cl ≈ Br. We showed theoretical evidence (cf. Figure 8) that this detectable uranyl−F bond covalency is very likely due to the good energy match between uranyl and F valence orbitals, with implications for the stability of the complex with F.

Experimentally, the energy shifts of the U 4f XPS peaks (Figure S17) and the U M_4 edge HR-XANES (RIXS) absorption edge (Figure S5) give insights into the electron density on U. Being shifted to higher binding/photon energies for uranyl fluoride, they suggest a reduced electron density on U for the F compound. This gives experimental evidence for larger bond covalency (and therefore donation of electron density) for uranyl bromide and chloride compared to uranyl fluoride, in close agreement with the computational bond analysis.

Figure 7b shows that the CVI and the total orbital overlap for localized valence orbitals are inversely correlated to the U−O bond length, suggesting a direct relationship between the bond covalency and length for these uranyl compounds. This is expected to also correlate with the separation between the LUMO and the σ^* orbital. Often, the A−C peak separation in HR-XANES is used as a measure for this effect. Here, such a correlation is not found, and we are able to explain this by the differences between ground state and RIXS final state energies. This finding illustrates that the A−C separation should be used with caution when comparing uranyl bond length or covalency for compounds with different equatorial coordination and electronic structure.

Finally, we link the bonding characteristics of uranyl halides to the affinity of the uranyl halides. As mentioned, previous

studies have identified the stronger overall bonding between U and F, versus U and Cl/Br,[9] despite the lower covalency in the U−F bond. We verified this finding by EXAFS studies on aqueous complexes, which demonstrated higher UO_2^{2+}-F^- and PuO_2^{2+}-F^- complexation even at lower F^-_{aq} concentrations. In the solid phase, this significantly higher affinity for F^- ligands, in combination with the significantly smaller ionic radius of F^- compared to Cl^- and Br^-, results in a much shorter U−X bond distance in the structure of F compounds (compared to Cl and Br compounds). Combined with the increased equatorial coordination (4 vs 5), this could lead to a steric influence on the uranyl bond length; the highly coordinated, close F ions effectively are 'pushing' the uranyl oxygens further away from the U center. This may contribute to the longer U═O bond in the fluoride compound.

CONCLUSIONS

We have presented a comprehensive investigation of uranyl halide compounds, demonstrating how the electronic structure of these compounds and the covalency of the U═O axial and U−X equatorial bonds change from F to Br. These results are supported by a multitechnique, experimental, and computational approach. We find that the uranyl−X bond covalency exists in all three investigated compounds. A new measure for covalency defined in this study, the CVI, and the orbital overlap of localized orbitals for U−O and U−X, follows the trend Cl ≈ Br > F for the investigated compounds. The same trend is followed when the total uranium-ligand bond covalency is evaluated; it decreases in the order Cl ≈ Br > F and is inversely correlated with the U−O bond length.

Significant differences have been resolved in the electronic structures of the three compounds, with the HOMOs of the F compound being of mixed character (a2″), whereas the Cl and Br compounds show predominantly ligand p character (a2g) in the HOMOs. This difference could enhance the "pushing-from-below" effect in the F system due to an enhanced 5f character in the HOMO. This electronic effect is likely to be responsible for destabilizing and elongating the U−O axial bond. Steric effects resulting from the short U−F bond length can also not be excluded.

The character of the HOMO manifests itself experimentally in a large energy separation of the A and C resonances in the $NaRb_8(UO_2)_5F_{19}\cdot 2H_2O$ U M_4 edge HR-XANES (RIXS) spectra. We have shown that the A−C separation trends are not directly usable as a tool for probing the axial bond length and bond covalency for the uranyl halide series. The excited state RIXS calculations, based on LFDFT, successfully reproduce the experimental spectra. In contrast, TDDFT calculations are best used to describe XANES spectra, which average over the different available decay channels and are characterized by a final state different from that in the RIXS case.

It is demonstrated that the affinity of uranyl and plutonyl in solution is the highest for the fluoride system. This result suggests that there is a larger uranyl-F total bond strength, which is likely due to the incidental increase in uranyl−F bond covalency as a result of good energy matching, in combination with the greater ionic strength of the uranyl−F bond compared to the uranyl−Cl/Br bond. This finding is also applicable to Pu systems. Comparative follow-up studies involving the substitution of uranium with plutonium in isostructural solid compounds, which will alter the energy match, can provide further insights into elucidating the most important electronic and bonding effects influencing the actinyl-halide bond stability.

Finally, this investigation demonstrates a bonding analysis approach that combines advanced experimental and theoretical tools applicable to all actinide elements. Our results will stimulate the discussion of the role of the equatorial ligands for tuning electronic structure and bonding properties of uranyl and generally actinyls and provide guidance for exploiting the opportunities of novel reaction pathways.

Accession Codes

Deposition Numbers 2325073 and 2325086−2325087 contain the supplementary crystallographic data for this paper. These data can be obtained free of charge via the joint Cambridge Crystallographic Data Centre (CCDC) and Fachinformationszentrum Karlsruhe Access Structures service.

AUTHOR INFORMATION

Corresponding Authors

Thomas S. Neill − *Institute for Nuclear Waste Disposal (INE), Karlsruhe Institute of Technology (KIT), 76131 Karlsruhe, Germany; Radioactive Waste Disposal and Environmental Remediation (RADER), National Nuclear User Facility and Williamson Research Centre, Department of Earth & Environmental Sciences, The University of Manchester, Manchester M13 9PL, U.K.;* orcid.org/0000-0002-4316-1328; Email: thomas.neill@manchester.ac.uk

Harry Ramanantoanina − *Institute for Nuclear Waste Disposal (INE), Karlsruhe Institute of Technology (KIT), 76131 Karlsruhe, Germany;* Email: harry.ramanantoanina@kit.edu

Florian Weigend − *Institute for Quantum Materials and Technologies (IQMT), Karlsruhe Institute of Technology (KIT), 76131 Karlsruhe, Germany;* orcid.org/0000-0001-5060-1689; Email: florian.weigend@kit.edu

Tonya Vitova − *Institute for Nuclear Waste Disposal (INE), Karlsruhe Institute of Technology (KIT), 76131 Karlsruhe, Germany;* orcid.org/0000-0002-3117-7701; Email: tonya.vitova@kit.edu

Authors

Natalia Palina − *Institute for Nuclear Waste Disposal (INE), Karlsruhe Institute of Technology (KIT), 76131 Karlsruhe, Germany*

Tim Prüßmann − *Institute for Nuclear Waste Disposal (INE), Karlsruhe Institute of Technology (KIT), 76131 Karlsruhe, Germany;* orcid.org/0000-0002-7903-9199

Jörg Rothe − *Institute for Nuclear Waste Disposal (INE), Karlsruhe Institute of Technology (KIT), 76131 Karlsruhe, Germany;* orcid.org/0000-0001-5366-2129

Xavier Gaona − *Institute for Nuclear Waste Disposal (INE), Karlsruhe Institute of Technology (KIT), 76131 Karlsruhe, Germany;* orcid.org/0000-0002-0787-200X

David Fellhauer − *Institute for Nuclear Waste Disposal (INE), Karlsruhe Institute of Technology (KIT), 76131 Karlsruhe, Germany;* orcid.org/0000-0002-7440-0790

Dieter Schild − *Institute for Nuclear Waste Disposal (INE), Karlsruhe Institute of Technology (KIT), 76131 Karlsruhe, Germany;* orcid.org/0000-0001-6034-8146
Constantin Wansorra − *Institute for Photon Science and Synchrotron Radiation (IPS), Karlsruhe Institute of Technology (KIT), 76131 Karlsruhe, Germany; Department of Chemistry and Biochemistry, University of Nevada, Las Vegas (UNLV), Las Vegas, Nevada 89154-4003, United States;* orcid.org/0000-0002-7120-8322
Dirk Hauschild − *Institute for Photon Science and Synchrotron Radiation (IPS) and Institute for Chemical Technology and Polymer Chemistry (ITCP), Karlsruhe Institute of Technology (KIT), 76131 Karlsruhe, Germany; Department of Chemistry and Biochemistry, University of Nevada, Las Vegas (UNLV), Las Vegas, Nevada 89154-4003, United States;* orcid.org/0000-0001-9088-8944
Ralph Steininger − *Institute for Photon Science and Synchrotron Radiation (IPS), Karlsruhe Institute of Technology (KIT), 76131 Karlsruhe, Germany*
Bianca Schacherl − *Institute for Nuclear Waste Disposal (INE), Karlsruhe Institute of Technology (KIT), 76131 Karlsruhe, Germany;* orcid.org/0000-0003-4542-0108
Clemens Heske − *Institute for Photon Science and Synchrotron Radiation (IPS) and Institute for Chemical Technology and Polymer Chemistry (ITCP), Karlsruhe Institute of Technology (KIT), 76131 Karlsruhe, Germany; Department of Chemistry and Biochemistry, University of Nevada, Las Vegas (UNLV), Las Vegas, Nevada 89154-4003, United States;* orcid.org/0000-0001-7586-4549
Lothar Weinhardt − *Institute for Photon Science and Synchrotron Radiation (IPS) and Institute for Chemical Technology and Polymer Chemistry (ITCP), Karlsruhe Institute of Technology (KIT), 76131 Karlsruhe, Germany; Department of Chemistry and Biochemistry, University of Nevada, Las Vegas (UNLV), Las Vegas, Nevada 89154-4003, United States;* orcid.org/0000-0003-3361-1054
Olaf Walter − *European Commission, Joint Research Centre Karlsruhe (JRC), 76344 Eggenstein-Leopoldshafen, Germany;* orcid.org/0000-0002-2679-1715

Notes

The authors declare no competing financial interest.

ACKNOWLEDGMENTS

The authors gratefully acknowledge funding from the European Research Council (ERC) Consolidator Grant 2020 under the European Union's Horizon 2020 research and innovation program (Grant Agreement 101003292). The authors thank the Institute for Beam Physics and Technology (IBPT, KIT) for the operation of the Karlsruhe Research Accelerator (KARA) for the KIT Light Source. T. S. Neill acknowledges EPSRC for funding under the EP/X036065/1 fellowship grant. The authors also acknowledge high performance computing (HPC) support, time, and infrastructure provided by the Baden-Württemberg HPC facility BWUniCluster. The authors thank Ivan Pidchenko and Alisa Prokopchuk for preliminary work on these systems.

REFERENCES

(1) Pepper, M.; Bursten, B. E. The electronic structure of actinide-containing molecules: a challenge to applied quantum chemistry. *Chem. Rev.* **1991**, *91* (5), 719−741.
(2) Neidig, M. L.; Clark, D. L.; Martin, R. L. Covalency in f-element complexes. *Coord. Chem. Rev.* **2013**, *257* (2), 394−406.
(3) Vitova, T.; Pidchenko, I.; Fellhauer, D.; Bagus, P. S.; Joly, Y.; Pruessmann, T.; Bahl, S.; Gonzalez-Robles, E.; Rothe, J.; Altmaier, M.; et al. The role of the 5f valence orbitals of early actinides in chemical bonding. *Nat. Commun.* **2017**, *8*, 16053.
(4) Altmaier, M.; Gaona, X.; Faenghanel, T. Recent advances in aqueous actinide chemistry and thermodynamics. *Chem. Rev.* **2013**, *113* (2), 901−943.
(5) Geckeis, H.; Luetzenkirchen, J.; Polly, R.; Rabung, T.; Schmidt, M. Mineral-water interface reactions of actinides. *Chem. Rev.* **2013**, *113* (2), 1016−1062.
(6) Denning, R. G.; Green, J. C.; Hutchings, T. E.; Dallera, C.; Tagliaferri, A.; Giarda, K.; Brookes, N. B.; Braicovich, L. Covalency in the uranyl ion: A polarized x-ray spectroscopic study. *J. Chem. Phys.* **2002**, *117* (17), 8008−8020.
(7) Denning, R. G. Electronic structure and bonding in actinyl ions and their analogs. *J. Phys. Chem. A* **2007**, *111* (20), 4125−4143.
(8) Spencer, L. P.; Yang, P.; Minasian, S. G.; Jilek, R. E.; Batista, E. R.; Boland, K. S.; Boncella, J. M.; Conradson, S. D.; Clark, D. L.; Hayton, T. W.; et al. Tetrahalide complexes of the $[U(NR)_2]^{2+}$ ion: synthesis, theory, and chlorine K-edge X-ray absorption spectroscopy. *J. Am. Chem. Soc.* **2013**, *135* (6), 2279−2290.
(9) Su, J.; Dau, P. D.; Qiu, Y. H.; Liu, H. T.; Xu, C. F.; Huang, D. L.; Wang, L. S.; Li, J. Probing the electronic structure and chemical bonding in tricoordinate uranyl complexes $UO_2X_3^-$ (X = F, Cl, Br, I): competition between Coulomb repulsion and U-X bonding. *Inorg. Chem.* **2013**, *52* (11), 6617−6626.
(10) Vitova, T.; Faizova, R.; Amaro-Estrada, J. I.; Maron, L.; Pruessmann, T.; Neill, T.; Beck, A.; Schacherl, B.; Tirani, F. F.; Mazzanti, M. The mechanism of Fe induced bond stability of uranyl(V). *Chem. Sci.* **2022**, *13* (37), 11038−11047.
(11) Vitova, T.; Green, J. C.; Denning, R. G.; Loble, M.; Kvashnina, K.; Kas, J. J.; Jorissen, K.; Rehr, J. J.; Malcherek, T.; Denecke, M. A. Polarization dependent high energy resolution X-ray absorption study of dicesium uranyl tetrachloride. *Inorg. Chem.* **2015**, *54* (1), 174−182.
(12) Ramanantoanina, H.; Kuri, G.; Martin, M.; Bertsch, J. Study of electronic structure in the L-edge spectroscopy of actinide materials: UO_2 as an example. *Phys. Chem. Chem. Phys.* **2019**, *21* (15), 7789−7801.
(13) Bagus, P. S.; Schacherl, B.; Vitova, T. Computational and Spectroscopic Tools for the Detection of Bond Covalency in Pu(IV) Materials. *Inorg. Chem.* **2021**, *60* (21), 16090−16102.
(14) Konecny, L.; Vicha, J.; Komorovsky, S.; Ruud, K.; Repisky, M. Accurate X-ray Absorption Spectra near L- and M-Edges from Relativistic Four-Component Damped Response Time-Dependent Density Functional Theory. *Inorg. Chem.* **2022**, *61* (2), 830−846.
(15) Sergentu, D. C.; Autschbach, J. X-ray absorption spectra of f-element complexes: insight from relativistic multiconfigurational wavefunction theory. *Dalton Trans* **2022**, *51* (5), 1754−1764.
(16) Sergentu, D. C.; Autschbach, J. Covalency in actinide(IV) hexachlorides in relation to the chlorine K-edge X-ray absorption structure. *Chem. Sci.* **2022**, *13* (11), 3194−3207.
(17) Stanistreet-Welsh, K.; Kerridge, A. Bounding $[AnO_2]^{2+}$ (An = U, Np) covalency by simulated O K-edge and An M-edge X-ray absorption near-edge spectroscopy. *Phys. Chem. Chem. Phys.* **2023**, *25* (35), 23753−23760.
(18) Misael, W. A.; Severo Pereira Gomes, A. Core Excitations of Uranyl in $Cs_2UO_2Cl_4$ from Relativistic Embedded Damped Response Time-Dependent Density Functional Theory Calculations. *Inorg. Chem.* **2023**, *62* (29), 11589−11601.
(19) Bagus, P. S.; Nelin, C. J.; Rosso, K. M.; Schacherl, B.; Vitova, T. Electronic Structure of Actinyls: Orbital Properties. *Inorg. Chem.* **2024**, *63* (4), 1793−1802.

(20) Ehrman, J. N.; Shumilov, K.; Jenkins, A. J.; Kasper, J. M.; Vitova, T.; Batista, E. R.; Yang, P.; Li, X. Unveiling Hidden Shake-Up Features in the Uranyl M_4-Edge Spectrum. *JACS Au* **2024**, *4* (3), 1134−1141.
(21) Butorin, S. M. 3d-4f Resonant Inelastic X-ray Scattering of Actinide Dioxides: Crystal-Field Multiplet Description. *Inorg. Chem.* **2020**, *59* (22), 16251−16264.
(22) Bagus, P. S.; Nelin, C. J.; Schacherl, B.; Vitova, T. Actinyl Electronic Structure Probed by XAS: The Role of Many-Body Effects. *Inorg. Chem.* **2024**, *63* (29), 13202−13213.
(23) Bagus, P. S.; Nelin, C. J.; Schacherl, B.; Vitova, T.; Polly, R. Bonding and Interactions in $UO(2)^{2+}$ for Ground and Core Excited States: Extracting Chemistry from Molecular Orbital Calculations. *J. Phys. Chem. A* **2024**, *128* (38), 8024−8034.
(24) Schacherl, B.; Tagliavini, M.; Kaufmann-Heimeshoff, H.; Göttlicher, J.; Mazzanti, M.; Popa, K.; Walter, O.; Pruessmann, T.; Vollmer, C.; Beck, A.; et al. Resonant inelastic X-ray scattering tools to count 5 f electrons of actinides and probe bond covalency. *Nat. Commun.* **2025**, *16* (1), 1221.
(25) Burrow, T. G.; Alcock, N. M.; Huzan, M. S.; Dunstan, M. A.; Seed, J. A.; Detlefs, B.; Glatzel, P.; Hunault, M.; Bendix, J.; Pedersen, K. S.; et al. Determination of Uranium Central-Field Covalency with 3d4f Resonant Inelastic X-ray Scattering. *J. Am. Chem. Soc.* **2024**, *146* (32), 22570−22582.
(26) Polly, R.; Schacherl, B.; Rothe, J.; Vitova, T. Relativistic Multiconfigurational Ab Initio Calculation of Uranyl 3d4f Resonant Inelastic X-ray Scattering. *Inorg. Chem.* **2021**, *60* (24), 18764−18776.
(27) Podkovyrina, Y.; Pidchenko, I.; Prüßmann, T.; Bahl, S.; Göttlicher, J.; Soldatov, A.; Vitova, T. Probing Covalency in the UO_3 Polymorphs by U M_4 edge HR-XANES. *Journal of Physics: Conference Series* **2016**, *712*, 012092.
(28) Vitova, T.; Pidchenko, I.; Biswas, S.; Beridze, G.; Dunne, P. W.; Schild, D.; Wang, Z.; Kowalski, P. M.; Baker, R. J. Dehydration of the Uranyl Peroxide Studtite, $[UO_2(n^2\text{-}O_2)(H_2O)_2]\cdot 2H_2O$, Affords a Drastic Change in the Electronic Structure: A Combined X-ray Spectroscopic and Theoretical Analysis. *Inorg. Chem.* **2018**, *57* (4), 1735−1743.
(29) Vitova, T.; Pidchenko, I.; Schild, D.; Prussmann, T.; Montoya, V.; Fellhauer, D.; Gaona, X.; Bohnert, E.; Rothe, J.; Baker, R. J.; et al. Competitive Reaction of Neptunium(V) and Uranium(VI) in Potassium-Sodium Carbonate-Rich Aqueous Media: Speciation Study with a Focus on High-Resolution X-ray Spectroscopy. *Inorg. Chem.* **2020**, *59* (1), 8−22.
(30) Hunault, M. O. J. Y.; Menut, D.; Tougait, O. Alkali Uranyl Borates: Bond Length, Equatorial Coordination and 5f States. *Crystals* **2021**, *11* (1), 56.
(31) Amidani, L.; Retegan, M.; Volkova, A.; Popa, K.; Martin, P. M.; Kvashnina, K. O. Probing the Local Coordination of Hexavalent Uranium and the Splitting of 5f Orbitals Induced by Chemical Bonding. *Inorg. Chem.* **2021**, *60* (21), 16286−16293.
(32) Pepper, M.; Bursten, B. E. The electronic structure of actinide-containing molecules: a challenge to applied quantum chemistry. *Chem. Rev.* **1991**, *91* (5), 719−741.
(33) Dyall, K. G. Bonding and bending in the actinyls. *Mol. Phys.* **1999**, *96* (4), 511−518.
(34) Kaltsoyannis, N. Computational study of analogues of the uranyl ion containing the -N=U=N- unit: density functional theory calculations on UO_2^{2+}, UON^+, UN_2, $UO(NPH_3)^{3+}$, $U(NPH_3)_2^{4+}$, $[UCl_4[NPR_3]_2]$ (R = H, Me), and $[UOCl_4[NP(C_6H_5)_3]]$. *Inorg. Chem.* **2000**, *39* (26), 6009−6017.
(35) Tatsumi, K.; Hoffmann, R. Bent cis d^0 MoO_2^{2+} vs. linear trans d^0f^0 UO_2^{2+}: a significant role for nonvalence 6p orbitals in uranyl. *Inorg. Chem.* **1980**, *19* (9), 2656−2658.
(36) Brusset, H.; Nguyen-Quy, D.; Rubinstein-Auban, A. Structure cristalline de $Rb_2UO_2F_4\cdot H_2O$. *Acta Crystallogr., Sect. B:Struct. Sci.* **1972**, *28* (8), 2617−2619.
(37) Wilson, R. E.; Skanthakumar, S.; Cahill, C. L.; Soderholm, L. Structural studies coupling X-ray diffraction and high-energy X-ray scattering in the UO_2^{2+}-HBr_{aq} system. *Inorg. Chem.* **2011**, *50* (21), 10748−10754.
(38) Schnaars, D. D.; Wilson, R. E. Structural and vibrational properties of $U(VI)O_2Cl_4^{2-}$ and $Pu(VI)O_2Cl_4^{2-}$ complexes. *Inorg. Chem.* **2013**, *52* (24), 14138−14147.
(39) Kozimor, S. A.; Yang, P.; Batista, E. R.; Boland, K. S.; Burns, C. J.; Christensen, C. N.; Clark, D. L.; Conradson, S. D.; Hay, P. J.; Lezama, J. S.; et al. Covalency trends in group IV metallocene dichlorides. Chlorine K-edge X-ray absorption spectroscopy and time dependent-density functional theory. *Inorg. Chem.* **2008**, *47* (12), 5365−5371.
(40) Kozimor, S. A.; Yang, P.; Batista, E. R.; Boland, K. S.; Burns, C. J.; Clark, D. L.; Conradson, S. D.; Martin, R. L.; Wilkerson, M. P.; Wolfsberg, L. E. Trends in covalency for d- and f-element metallocene dichlorides identified using chlorine K-edge X-ray absorption spectroscopy and time-dependent density functional theory. *J. Am. Chem. Soc.* **2009**, *131* (34), 12125−12136.
(41) Minasian, S. G.; Keith, J. M.; Batista, E. R.; Boland, K. S.; Clark, D. L.; Conradson, S. D.; Kozimor, S. A.; Martin, R. L.; Schwarz, D. E.; Shuh, D. K.; et al. Determining relative f and d orbital contributions to M-Cl covalency in MCl_6^{2-} (M = Ti, Zr, Hf, U) and $UOCl_5^-$ using Cl K-edge X-ray absorption spectroscopy and time-dependent density functional theory. *J. Am. Chem. Soc.* **2012**, *134* (12), 5586−5597.
(42) Hu, Z.; Kaindl, G.; Meyer, G. Chemical shifts in the X-ray absorption near-edge structure spectra of UBr_n (n=3, 4, 5) and Cs_2LiUX_6 (X=F, Cl, Br, I). *J. Alloys Compd.* **1998**, *274* (1−2), 38−41.
(43) Su, J.; Batista, E. R.; Boland, K. S.; Bone, S. E.; Bradley, J. A.; Cary, S. K.; Clark, D. L.; Conradson, S. D.; Ditter, A. S.; Kaltsoyannis, N.; et al. Energy-Degeneracy-Driven Covalency in Actinide Bonding. *J. Am. Chem. Soc.* **2018**, *140* (51), 17977−17984.
(44) Sergentu, D. C.; Gendron, F.; Walter, E. D.; Park, S.; Capan, C.; Surbella, R. G.; Soderquist, C. Z.; Hall, G. B.; Sinkov, S. I.; Autschbach, J.; et al. Equatorial Electronic Structure in the Uranyl Ion: $Cs_2UO_2Cl_4$ and $Cs_2UO_2Br_4$. *Inorg. Chem.* **2022**, *61* (9), 3821−3831.
(45) Rothe, J.; Butorin, S.; Dardenne, K.; Denecke, M. A.; Kienzler, B.; Loble, M.; Metz, V.; Seibert, A.; Steppert, M.; Vitova, T.; et al. The INE-Beamline for actinide science at ANKA. *Rev. Sci. Instrum.* **2012**, *83* (4), 043105.
(46) Zimina, A.; Dardenne, K.; Denecke, M. A.; Doronkin, D. E.; Huttel, E.; Lichtenberg, H.; Mangold, S.; Pruessmann, T.; Rothe, J.; Spangenberg, T.; et al. CAT-ACT-A new highly versatile x-ray spectroscopy beamline for catalysis and radionuclide science at the KIT synchrotron light facility ANKA. *Rev. Sci. Instrum.* **2017**, *88* (11), 113113.
(47) Schacherl, B.; Prussmann, T.; Dardenne, K.; Hardock, K.; Krepper, V.; Rothe, J.; Vitova, T.; Geckeis, H. Implementation of cryogenic tender X-ray HR-XANES spectroscopy at the ACT station of the CAT-ACT beamline at the KIT Light Source. *J. Synchrotron Radiat.* **2022**, *29* (Part 1), 80−88.
(48) Weinhardt, L.; Steininger, R.; Kreikemeyer-Lorenzo, D.; Mangold, S.; Hauschild, D.; Batchelor, D.; Spangenberg, T.; Heske, C. X-SPEC: a 70 eV to 15 keV undulator beamline for X-ray and electron spectroscopies. *J. Synchrotron Radiat.* **2021**, *28* (Part 2), 609−617.
(49) Kotani, A.; Kvashnina, K. O.; Butorin, S. M.; Glatzel, P. A new method of directly determining the core-hole effect in the Ce L_3 XAS of mixed valence Ce compounds—An application of resonant X-ray emission spectroscopy. *J. Electron Spectrosc. Relat. Phenom.* **2011**, *184* (3−6), 210−215.
(50) Kotani, A.; Kvashnina, K. O.; Glatzel, P.; Parlebas, J. C.; Schmerber, G. Single impurity Anderson model versus density functional theory for describing Ce L_3 X-ray absorption spectra of $CeFe_2$: resolution of a recent controversy. *Phys. Rev. Lett.* **2012**, *108* (3), 036403.
(51) Kas, J. J.; Rehr, J. J.; Soininen, J. A.; Glatzel, P. Real-space Green's function approach to resonant inelastic X-ray scattering. *Phys. Rev. B* **2011**, *83* (23), 235114.

(52) Kvashnina, K. O.; Butorin, S. M.; Glatzel, P. Direct study of the f-electron configuration in lanthanide systems. *Journal of Analytical Atomic Spectrometry* **2011**, *26* (6), 1265−1272.
(53) Zegke, M.; Zhang, X.; Pidchenko, I.; Hlina, J. A.; Lord, R. M.; Purkis, J.; Nichol, G. S.; Magnani, N.; Schreckenbach, G.; Vitova, T.; et al. Differential uranyl(V) oxo-group bonding between the uranium and metal cations from groups 1, 2, 4, and 12; a high energy resolution X-ray absorption, computational, and synthetic study. *Chem. Sci.* **2019**, *10* (42), 9740−9751.
(54) Bordage, A.; Papai, M.; Sas, N. S.; Szlachetko, J.; Nachtegaal, M.; Vanko, G. On the sensitivity of hard X-ray spectroscopies to the chemical state of Br. *Phys. Chem. Chem. Phys.* **2013**, *15* (26), 11088−11098.
(55) Hazemann, J.-L.; Proux, O.; Brooker, R. A.; Cadoux, A.; Louvel, M. New insights on Br speciation in volcanic glasses and structural controls on halogen degassing. *Am. Mineral.* **2020**, *105* (6), 795−802.
(56) Mulliken, R. S. Electronic Population Analysis on LCAO-MO Molecular Wave Functions. I. *J. Chem. Phys.* **1955**, *23* (10), 1833−1840.
(57) Reed, A. E.; Weinstock, R. B.; Weinhold, F. Natural population analysis. *J. Chem. Phys.* **1985**, *83* (2), 735−746.
(58) Heinzmann, R.; Ahlrichs, R. Population analysis based on occupation numbers of modified atomic orbitals (MAOs). *Theoretica Chimica Acta* **1976**, *42* (1), 33−45.
(59) Singh, U. C.; Kollman, P. A. An approach to computing electrostatic charges for molecules. *J. Comput. Chem.* **1984**, *5* (2), 129−145.
(60) Pipek, J.; Mezey, P. G. A fast intrinsic localization procedure applicable for abinitio and semiempirical linear combination of atomic orbital wave functions. *J. Chem. Phys.* **1989**, *90* (9), 4916−4926.
(61) Motta, L. C.; Autschbach, J. Actinide inverse trans influence versus cooperative pushing from below and multi-center bonding. *Nat. Commun.* **2023**, *14* (1), 4307.
(62) Soderholm, L.; Skanthakumar, S.; Wilson, R. E. Structural correspondence between uranyl chloride complexes in solution and their stability constants. *J. Phys. Chem. A* **2011**, *115* (19), 4959−4967.
(63) Vallet, V.; Wahlgren, U.; Schimmelpfennig, B.; Moll, H.; Szabo, Z.; Grenthe, I. Solvent effects on uranium(VI) fluoride and hydroxide complexes studied by EXAFS and quantum chemistry. *Inorg. Chem.* **2001**, *40* (14), 3516−3525.